Materialia 14 (2020) 100917

Contents lists available at ScienceDirect

Materialia

journal homepage: www.elsevier.com/locate/mtla

Full Length Article

Microstructural homogenization and substantial improvement in corrosion resistance of mechanically alloyed FeCoCrNiCu high entropy alloys by incorporation of carbon nanotubes

Sujata Singh[a], Sufyan M. Shaikh[b], Punith Kumar M K[a], B.S. Murty[b,c], Chandan Srivastava[a,*]

[a] Department of Materials Engineering, Indian Institute of Science, Bangalore 560012, India
[b] Department of Metallurgical and Materials Engineering, Indian Institute of Technology, Chennai, Madras, India
[c] Indian Institute of Technology Hyderabad, Telangana, India

ARTICLE INFO

Keywords:
High entropy alloys
Carbon nanotubes
Corrosion
Homogenization
Microstructure

ABSTRACT

FeCoCrNiCu high entropy alloy (HEA) powder was produced by mechanical alloying. Carbon Nanotubes (CNTs) were mixed in the HEA powder (0.1, 0.2, 0.5, 1.0, 1.5, 2.0, 3.0, 5.0, 7.0 wt.% of CNT) and then the mixture was consolidated by spark plasma sintering at 800°C. Phase constitution of the pellets was sensitive to the CNT amount. With smaller quantities of CNTs (upto 2 wt.%), the pellets contained a mixture of two different face centred cubic (fcc) phases along with σ phase. With increase in the CNT amount (till 2 wt.%), a gradual decrease in the volume fraction of one of the fcc phase occurred leading to microstructural homogenization. Higher CNT additions (3, 5 and 7 wt.%) led to re-evolution of inhomogeneous microstructure containing chromium carbide phase and the two different fcc phases. Corrosion behaviour measurements showed that with continued addition of CNTs, reduction in the corrosion rate happened till 2wt.% CNT. Beyond this, a significant enhancement in the corrosion rate was noticed for pellets with 3, 5 and 7 wt.% CNT additions. Between the pristine HEA pellet and the pellet with optimum CNT amount (2 wt.%), 88.6 % reduction in the corrosion rate was measured. The enhancement in the corrosion resistance was attributed to an increase in the chemical homogeneity, which reduced the possibility of galvanic coupling. The decrease in the corrosion resistance beyond the optimum CNT (2 wt.%) was attributed to the re-appearance of chemical heterogeneity and evolution of chromium carbide ($Cr_{23}C_6$) phase, which causes intergranular corrosion in these systems.

1. Introduction

High Entropy alloys (HEAs) are radically different from the conventional alloy design perspective. HEAs contain five or more constituent elements in nearly equiatomic ratio [1,2]. The condition of maximizing configurational entropy for higher thermodynamic stability results in the evolution of multi-component solid solution structures in HEAs [3]. The interest in HEAs is due to their diverse properties of high corrosion resistance [4], superior oxidation properties [5,6], high-temperature strength [7], excellent wear resistance [8], high strength [9], fracture toughness [10], etc.

Mechanical alloying (MA) method is typically used for large-scale production of HEA powders [11]. The milled powders are subsequently compacted by spark plasma sintering (SPS) to produce high density sintered HEA pellets [12,13]. There are several reports on HEAs produced by MA followed by SPS (MA-SPS) where focus has primarily been on investigating the influence of alloying elements and heat treatment on phase evolution and mechanical properties [14-19]. Corrosion properties of HEAs produced by MA-SPS route remains scarcely explored.

Carbon nanotubes (CNTs) have been used as reinforcement in composites. Incorporation of CNTs leads to an increase in the corrosion resistance, thermal stability and hardness [20–26]. Most of the work on metal-CNT composites has been carried out on electrodeposited coatings, namely Ni-CNT [27], Ni-P-CNT [28], Mg-CNT [29], CuCr-CNT [30], Zn-Ni-CNT [31], Ni-Co-CNT [32] where a remarkable improvement in the corrosion resistance due to CNT addition has been noticed. There is no report available yet in the literature on the microstructure and corrosion properties of HEA-CNT composites.

In the present study, microstructure-corrosion property correlation has been investigated for FeCoCrNiCu HEA pellets containing different volume fraction of CNTs. FeCoCrNiCu HEA system has been chosen as the model matrix system as it satisfies the Hume-Rothery criterion for the formation of high entropy alloys (ΔS_{mix} = 1.61R J/mol K; ΔH_{mix} = 3.20 kJ/mol; δ = 1.07%).

* Corresponding author.
E-mail address: csrivastava@iisc.ac.in (C. Srivastava).

https://doi.org/10.1016/j.mtla.2020.100917
Received 26 June 2020; Accepted 28 September 2020
Available online 6 October 2020

2. Experimental procedure

2.1. Synthesis, functionalisation and purification of carbon nanotubes

Two gram of ferrocene (Alfa Aesar, 99% pure) was dissolved in 100 ml benzene under inert atmosphere via N_2 gas bubbling. The ferrocene–benzene solution was poured drop-wise (1 ml/min for 100 min) into quartz tube furnace maintained at 800°C. After the synthesis, the quartz tube was furnace-cooled under the inert atmosphere. The as-synthesized CNTs were scrapped from the walls of the quartz tube. The CNTs were washed with 10 % HCl solution to remove amorphous carbon and excess iron (from ferrocene). Washing was continued till the yellow coloured component (indicative of iron chloride) vanished from the refluxing solution. For functionalization, the CNTs were immersed in a mixture of H_2SO_4:HNO_3 (3:1) at room temperature and ultrasonicated for 2 hours. NH_4OH was used to neutralize this solution. The CNTs were then washed using deionized water until the neutral pH was achieved.

2.2. Mechanical alloying and spark plasma sintering of high entropy alloy

HEA powders were synthesised by ball milling. Appropriate amounts of elemental powders of Fe (0.5 gm), Ni (1.39 gm), Cr (0.8 gm), Co (1.6 gm), Cu (1.5 gm) with purity higher than 99.5% were used to produce nearly equiatomic composition. Planetary ball mill having stainless steel vials and balls was used for the MA. Milling was done at 300 rpm for 25 h with ball-to-powder ratio of 15:1 with toluene as the milling media. Functionalized CNTs were mixed with the milled metal powder and further ball-milled for 5 hours at 10:1 ball-to-powder ratio. Nine different HEA powder-CNT mixtures containing 0.1, 0.2, 0.5, 1.0, 1.5, 2.0, 3.0, 5.0, 7.0 wt.% of CNT were produced. The HEA and HEA-CNT mixture were then consolidated by SPS (Dr. Sinter SPS-5000, Fuji Electronic Industrial Co., Japan) using 15 mm diameter graphite punch and die at 800°C for 5 min at a pressure of 50 MPa to produce HEA-CNT pellets. The SPS parameter were chosen such that a high-density pellet with minimum grain growth and minimum degradation of the CNTs is obtained. The pellets containing 0, 0.1, 0.2, 0.5, 1.0, 1.5, 2.0, 3.0, 5.0, 7.0 wt.% of CNT are respectively referred as HEA, HEA_CNT1, HEA_CNT2, HEA_CNT3, HEA_CNT4, HEA_CNT5, HEA_CNT6, HEA_CNT7, HEA_CNT8 and HEA_CNT9.

2.3. Characterization

As-synthesized CNTs and phases in the milled and consolidated HEA samples were characterized from the X-ray diffraction (XRD) patterns obtained using X'pert pro diffractometer equipped with Cu-K_α (λ = 0.154 nm) radiation source. Pseudo-Voigt function was used for fitting the XRD peak profile and Si standard was used for instrumental broadening correction. The crystallite size and lattice strain were calculated by Williamson-Hall Equation [33]. Imaging and compositional analysis of the samples was conducted using the FEI Quanta scanning electron microscope (SEM) equipped with energy dispersive spectroscopy (EDS) detector. Raman spectrum from the CNTs was obtained using LabRam HR with a 532 nm laser. FTIR profile of as-synthesized CNTs were obtained using Bruker Tenor II instrument.

Electrochemical measurements were carried out using CHI 604E electrochemical set-up at room temperature. The HEA pellets with 2.2 cm^2 exposed area were used as the working electrode, platinum foil was used as the counter electrode and saturated Ag/AgCl electrode was used as the reference electrode for the corrosion studies in 3.5% NaCl solution. The open circuit potential (OCP) was evaluated for 3600 s and recorded. The Tafel curves or the potentiodynamic polarization curves were measured by polarizing the working electrode to ± 400 mV with respect to the OCP value at a scan rate of 1 mV s^{-1}. Electrochemical impedance studies were performed at the OCP value in the frequency range from 100 kHz to 0.01 Hz with the sinusoidal signal amplitude of 5 mV. The recorded EIS data for each of the samples were interpreted using the ZSimpWin 3.21 software and equivalent electrical circuits (EEC).

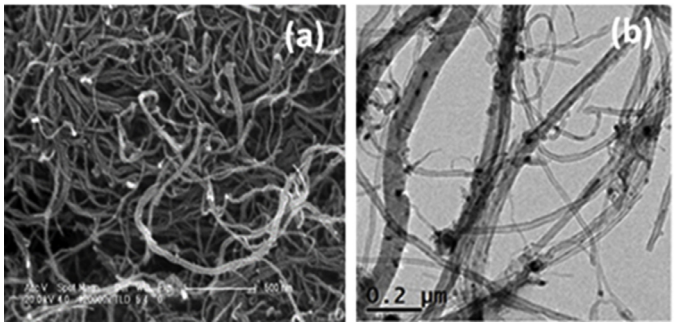

Fig. 1. (a) SEM image and (b) TEM image of functionalised CNTs.

3. Results and discussion

3.1. Characterization of CNTs

Representative SEM and TEM bright field micrograph of as-synthesized CNTs provided respectively in Fig. 1(a) and (b) reveal the formation of nanotube geometry. The CNTs produced were multi-walled with an average diameter of 27 nm ± 11nm. XRD profile obtained from the as-synthesized CNTs is provided in Fig. 2(a). The XRD profile shows the characteristic peaks at 2θ=26.1° and 2θ=43° corresponding to the reflections from (0 0 2) and (1 0 1) crystal planes. The prominent peak at 26.14° represents the (0 0 2) reflection of graphitic structure of the CNT [34]. Fig. 2(b) shows the Raman spectra obtained from the as-synthesized CNT. In the Raman spectra, D and G bands which are characteristic bands of graphitic structure correspond respectively to the sp^3 and sp^2 hybridized state of carbon [35]. The D band at around 1348 cm^{-1} is attributed to the disordered amorphous carbon structures, while the G band at about 1571 cm^{-1} corresponds to tangential vibrations of the graphite carbons (i.e. crystallinity). The second order Raman spectrum G' band at around 2683 cm^{-1} is due to the two-photon elastic scattering process. Fig. 2(c) shows the FTIR spectra that has three distinctive peaks (C=O, O-H, C-O) due to oxidation and formation of the COOH groups on the CNT surface during functionalization. The absorption band (in Fig, 2(c)) at 1757^{-1} cm, 3414^{-1} cm, 1053^{-1} cm and 1618^{-1} cm correspond to C=O stretching of COOH, O-H bending and C-O stretching, C=C stretching mode of carbon nanotubes respectively [35]. UV-Vis spectra obtained from the as-synthesized CNT is provided in Fig. 2(d). In the UV range of the spectrum at 272 nm absorption maxima are clearly observable while an adsorption band at 312 nm is present. The adsorption in the range of 200-350 nm is due to plasmon resonance in the free electron cloud of the CNT π-electrons multiwalled carbon nanotubes (MWCNTs) [36]. All the results above revealed the formation of CNTs.

3.2. Characterization of milled multi-component powders

Fig. 3(a) shows the XRD patterns of mechanically alloyed powders of FeCoCrNiCu as a function of the milling time. The diffraction peaks of individual elements observed at 0 hr disappeared after 30 hours of milling, indicating the formation of solid solution. One major face centered cubic (FCC) phase together with one minor body centered cubic (BCC) phase can be observed in Fig, 3(a). Broadening of peaks with increase in the milling time indicates towards formation of nanocrystalline grains. The appearance of nanocrystalline grains with milling time is in accordance with the reported results [37–39]. The BCC phase in the milled powder is expected to form due to the presence of chromium which is a BCC stabilizer and because of its high melting point it is not expected to dissolve much into the FCC phase [40,41]". A shift of the peaks towards

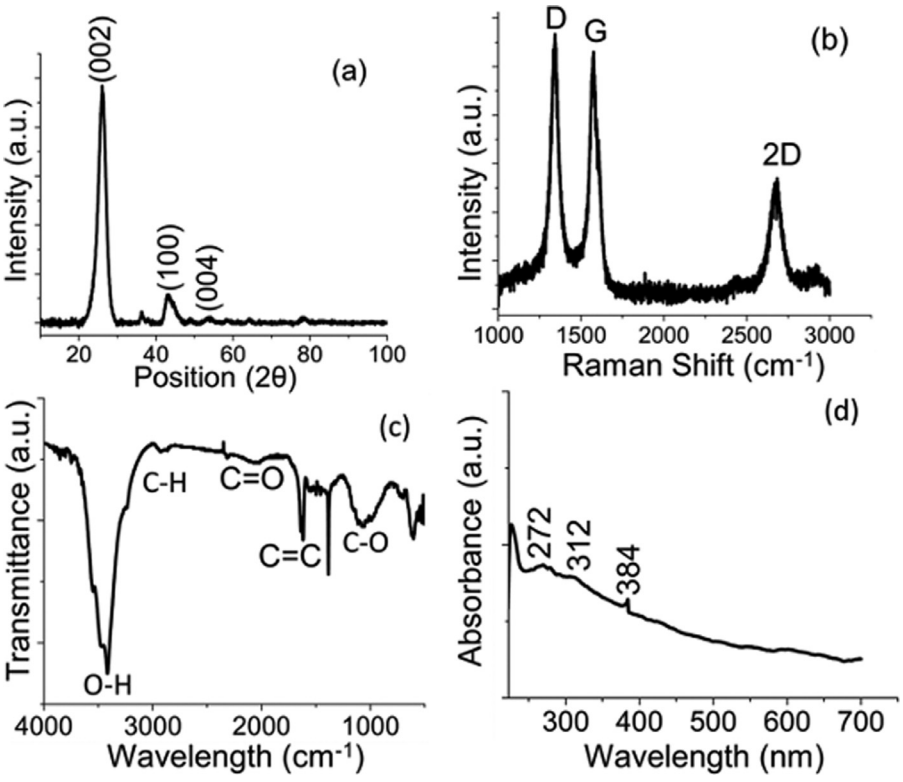

Fig. 2. (a) XRD Pattern, (b) Raman Spectra, (c) FTIR Spectrum and (d) UV-Vis spectroscopy of CNTs.

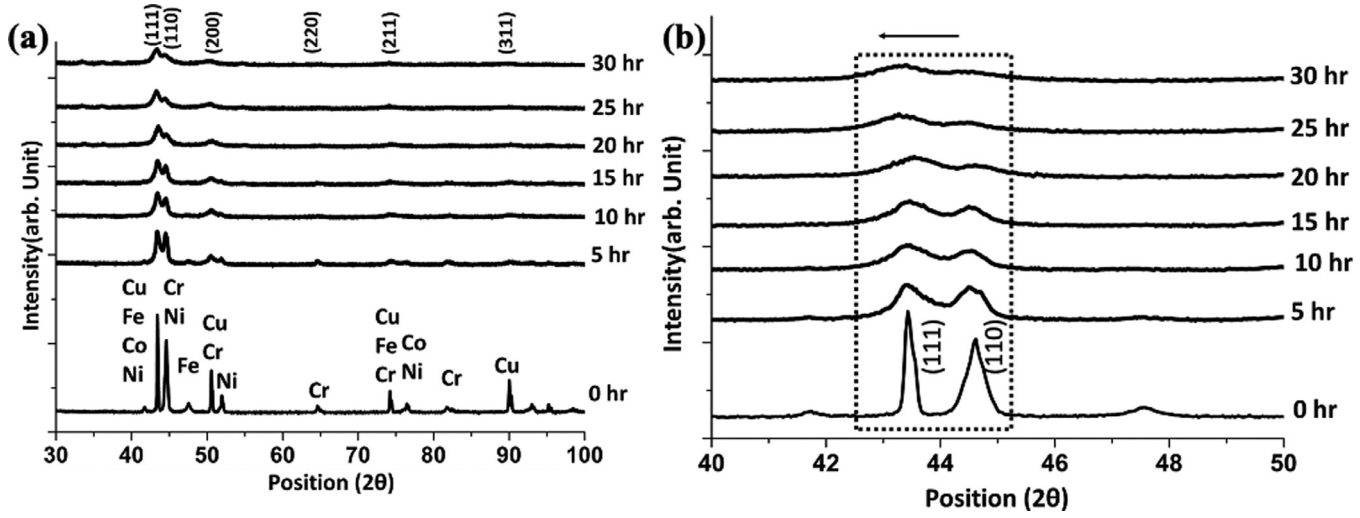

Fig. 3. (a) XRD pattern of mechanically alloyed HEAs and (b) Enlarged part of the pattern showing the shift in peaks.

lower 2-theta angles can be observed in Fig. 3(b) which re-plots the XRD curve in the 2-theta interval of 40-50^0. This shift in the Bragg angle is due to the residual stress in the powders because of mechanical milling. The reduction in the crystallite size and increase in the residual stress in the powders with milling time is provided in Table 1.

3.3. Phases constitution in spark plasma sintered HEA pellets

XRD profiles obtained from the spark plasma sintered HEA pellets containing CNTs is provided in Fig. 4(a–c). The XRD patterns illustrate formation of two FCC phases (denoted as F1 and F2) and a minor sigma phase (σ) in all the pellets. Sigma phase could be Co-Cr or Fe-Cr intermediate phase. Previous studies have also reported the formation of σ phase after sintering in Cr containing alloys [14,15,18,19,30]. The minor BCC phase formed after MA of powders disappeared with the formation of σ phase in HEA pellets. Praveen et al. [17] have reported transformation behavior from bcc to σ phase between 500°C and 600°C in HEAs. Formation of F2 FCC phase indicates Cu segregation because of its high

Table 1
Crystallite size and lattice strain of milled powder with respect to milling time.

Sample/milling time	Crystallite size (nm)	Strain %
0 hr	53.9	0.16
5 hr	31.1	0.27
10 hr	29.3	0.29
15 hr	24.2	0.32
20 hr	19.7	0.36
25 hr	17.8	0.54
30 hr	15.3	0.59

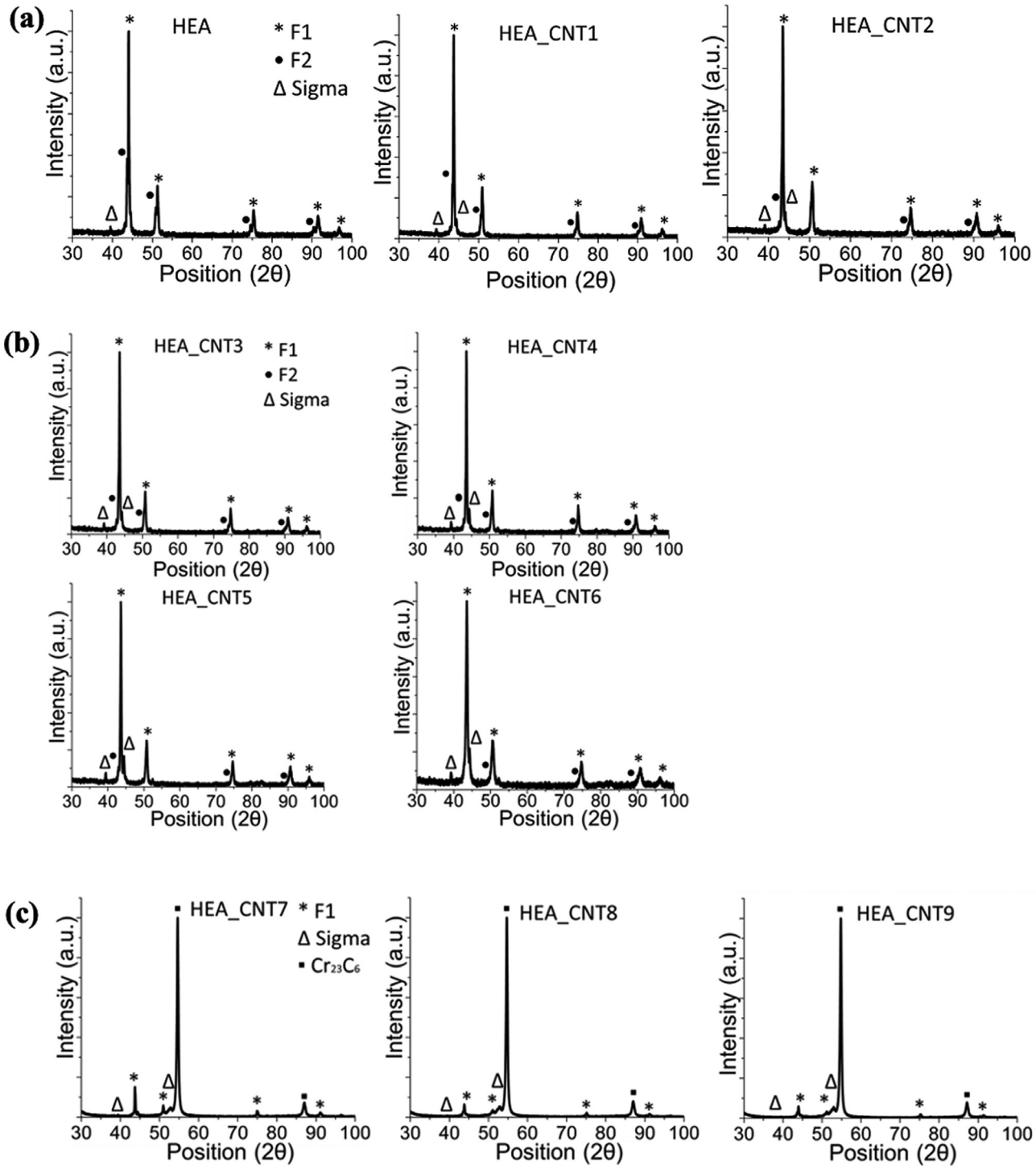

Fig. 4. XRD pattern of (a) HEA, HEA_CNT1, HEA_CNT2 samples, (b) HEA_CNT3, HEA_CNT4, HEA_CNT5, HEA_CNT6 samples and (c) HEA_CNT7, HEA_CNT8, HEA_CNT9 samples in the 2-theta range of 30–100.

enthalpy of mixing with other elements. Such observation is consistent with earlier reports on alloy systems containing Cu [11,13,14,17].

With increase in the volume fraction of CNTs, there was a reduction in the intensity of the F2 peak and a gradual homogenization of phases till HEA_CNT6. A drastic change in the phase constitution of the pellets, as revealed by the XRD pattern, was observed for HEA_ CNT7, HEA_CNT8 and HEA_CNT9 samples in Fig. 4(c). These pellets revealed very high fraction of chromium carbide phase as compared to the F1 and F2 phases. Interestingly, the initial homogenization achieved after the addition of CNTs in the pellets till HEA_CNT6 samples was reversed in case of HEA_CNT7, HEA_CNT8 and HEA_CNT9 samples where the F2 phase re-appeared. This is clear from the XRD curves in Fig. 5(a–c) plotted for 40°–50°, 2θ interval where F1 and F2 peak are clearly visible. Crystallite size and lattice strain values in the HEA and HEA_CNT pellets are tabulated in Table 2. Sintering of HEA and HEA_CNT powders led to an increase in the crystallite size and significant reduction in the lattice strain (when compared to 30 h milled powder sample) due to recovery and recrystallization of severely milled powders. It can however be noticed that addition of CNTs impedes these processes and therefore the crystallite sizes in HEA_CNT composite pellets are smaller

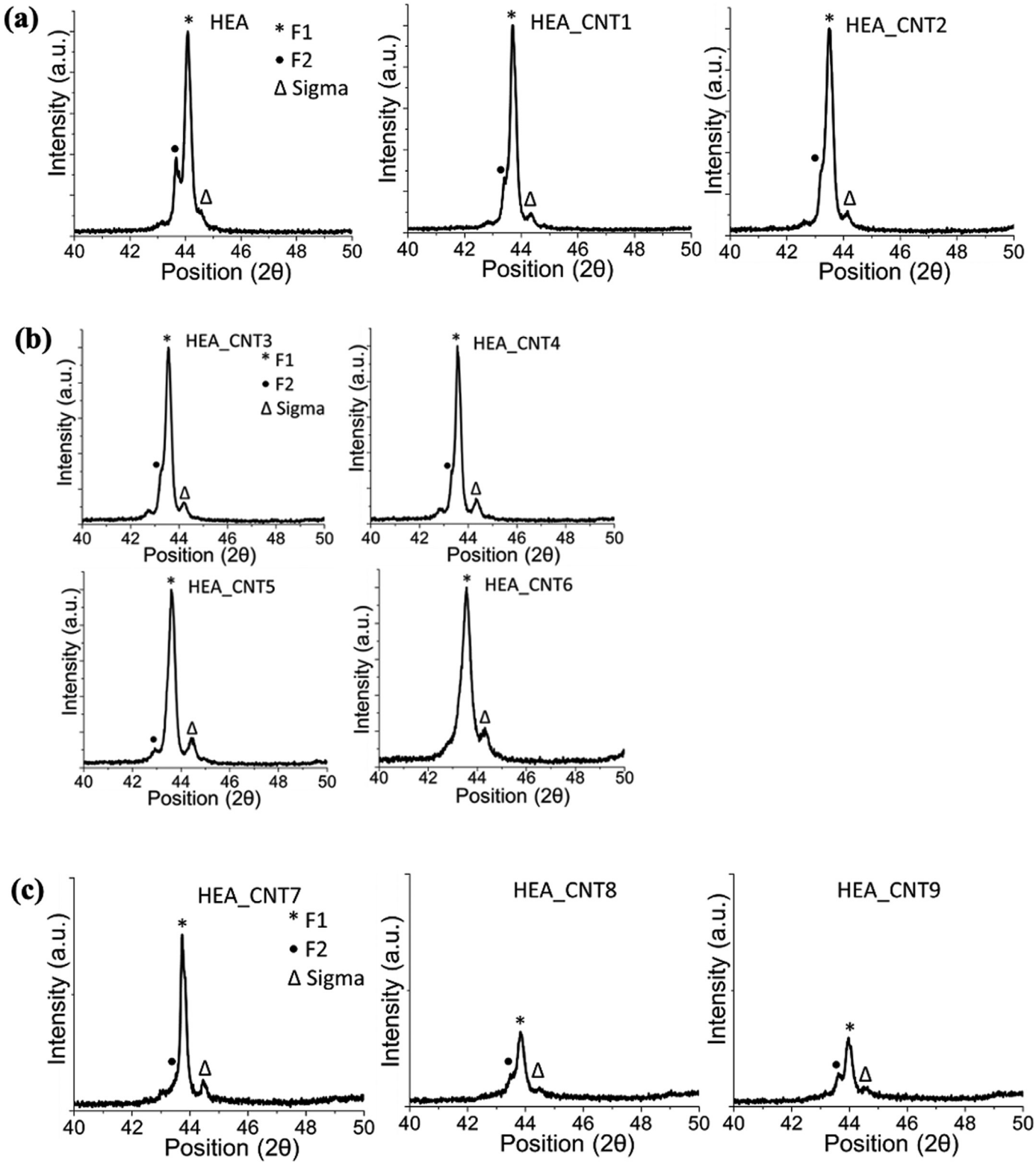

Fig. 5. XRD pattern of (a) HEA, HEA_CNT1, HEA_CNT2 samples, (b) HEA_CNT3, HEA_CNT4, HEA_CNT5, HEA_CNT6 samples and (c) HEA_CNT7, HEA_CNT8, HEA_CNT9 samples in the 2-theta range of 40–50.

and lattice strain values are higher when compared to the HEA pellet. This indicates the presence of more grain boundaries in the sample with higher CNT amounts. Higher grain boundary fraction and surface and cavity of the CNT tube can provide a shot-circuit path for elemental diffusion.

3.4. Microstructural characterization

3.4.1. Morphological changes during milling

Fig. 6 depicts the SEM images of the FeCoCrNiCu system at 0, 5, 10, 15, 20, 25 and 30 h of milling. The inset shows high magnification

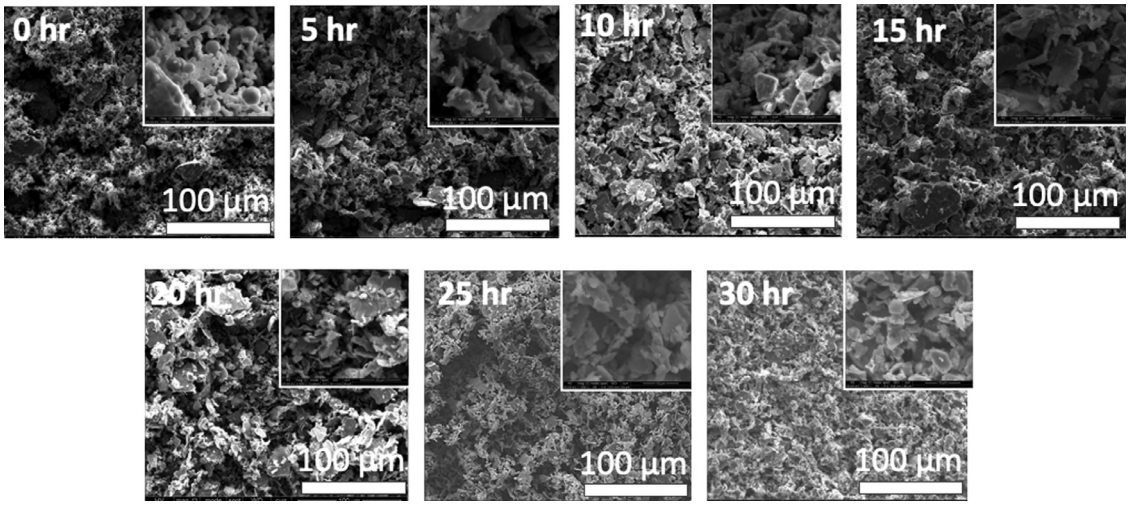

Fig. 6. SEM Micrographs showing morphological changes in HEA particles with respect to the milling time.

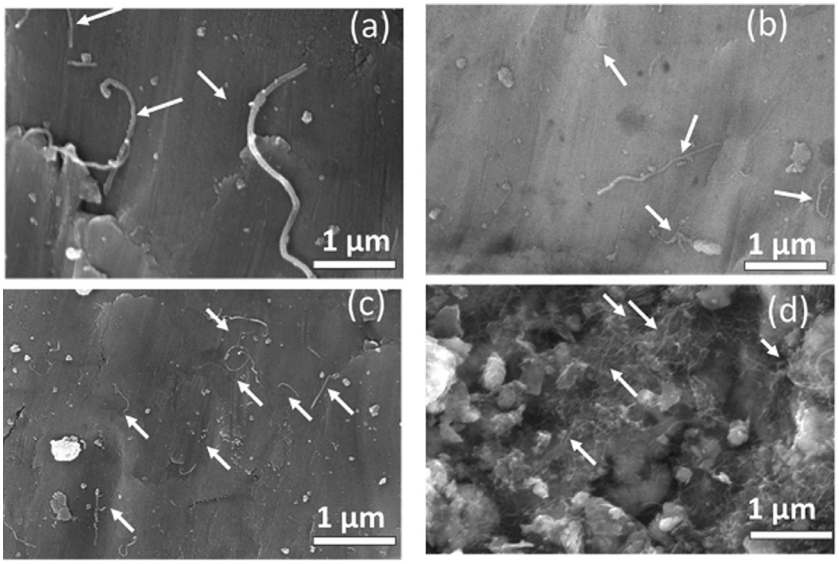

Fig. 7. Micrographs showing dispersion of CNT in (a) HEA_CNT2, (b) HEA_CNT3, (c) HEA_CNT6 and (d) HEA_CNT9.

Table 2
Crystallite size and lattice strain of sintered compacts.

Sample/wt% CNT	Crystallite Size (nm)	Strain %
HEA	49.3	0.13
HEA_CNT1	48.6	0.14
HEA_CNT2	47.2	0.17
HEA_CNT3	37.7	0.17
HEA_CNT4	37.4	0.18
HEA_CNT5	34.8	0.19
HEA_CNT6	31.7	0.19
HEA_CNT7	31.9	0.25
HEA_CNT8	33.6	0.21
HEA_CNT9	34.5	0.20

images. It can be observed from the images that the particle size reduced continuously with increase in the milling time. Initially, the particles are faceted, which is indicative of heavy deformation and fracturing. At the later stages of milling, flaky particles are observed whose volume fraction continuously increased.

3.4.3. Microstructure of sintered HEA pellets

Low magnification SEM micrographs showing the distribution of CNTs in sintered pellets is provided in Fig. 7. As observed in the images, CNT did not undergo significant damage or shortening and, as expected, the volume fraction of the CNTs increased from HEA_CNT2 and HEA_CNT9. A uniform distribution of CNTs in HEA_CNT6 can also be noticed. Theoretical density of the sintered pellets was calculated using rule of mixture of elemental densities and experimental density was measured using the Archimedes principle [42,43]. The density values provided in Table 3 show negligible change in the density of the pellets with the addition of MWCNTs. The bright and dark contrast regions in the SEM micrographs therefore correspond primarily to the different phases in the microstructure and are not due to differences in the amounts of pores in the microstructure.

Fig. 8(a–c) represents back-scattered electron (BSE) images of the pellets. A clear two-phase contrast can be observed in the micrographs (excluding the black portions which correspond to cavities). Spot compositional analysis showed that the brighter phase was copper-rich phase and the relatively darker phase was chromium-rich phase. The average composition of the brighter phase was Cr = 3.4±2.3; Fe = 8.7±3.3; Co = 7.2±2.6; Ni = 12.8±1.8 and Cu = 51.3±9.7 wt.% whereas the average composition of the darker phase was Cr = 60.1± 11.14; Fe = 7.7±2.1; Co = 8.7±3.9; Ni = 10.6±4.6; Cu = 6.9±2.8 wt.%. It can be also noticed (in Fig. 8) that with the addition of CNT, there is a progressive decrease in the phase separation (qualitatively revealed by increasing uniformity in the image contrast) till HEA_CNT6 sample indicating homogenization as also indicated by the XRD phase analysis and after HEA_CNT6 sample the phase separation again progressively

Table 3
Theoretical and relative density of HEA-CNT pellets.

Sample	HEA	HEA_CNT1	HEA_CNT2	HEA_CNT3	HEA_CNT4	HEA_CNT5	HEA_CNT6	HEA_CNT7	HEA_ CNT8	HEA_CNT9
Density	8.18	8.18	8.16	8.15	8.13	8.13	8.12	8.10	8.06	8.01
Relative density (%)	98.2	98.2	97.9	97.8	97.5	97.5	97.5	97.2	96.7	96.2

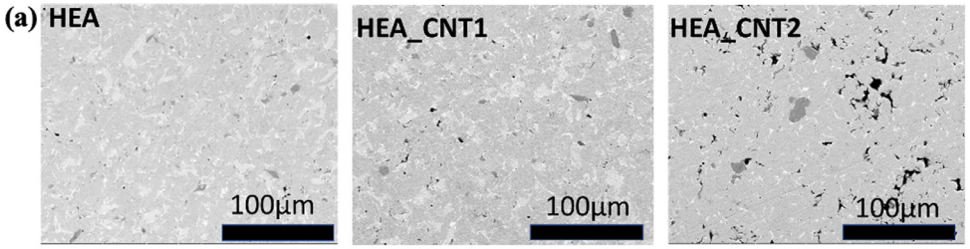

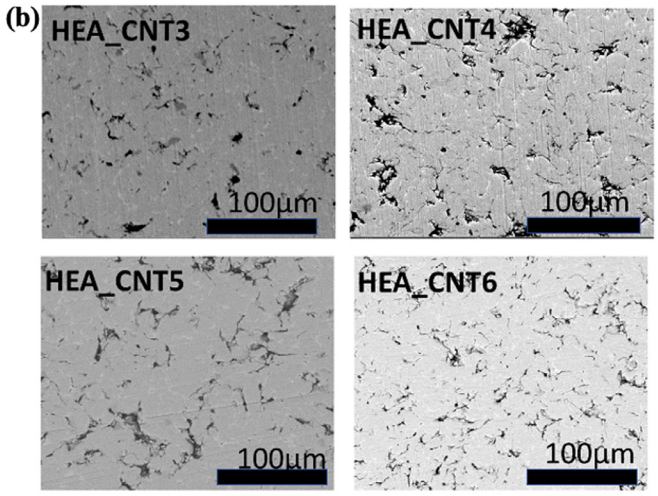

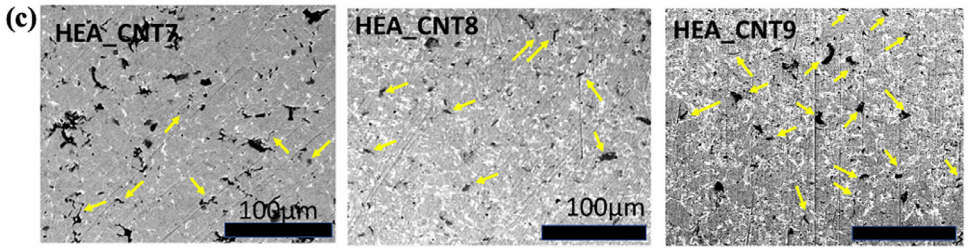

Fig. 8. SEM micrographs of (a) HEA, HEA_CNT1, HEA_CNT2 pellets, (b) HEA_CNT3, HEA_CNT4, HEA_CNT5, HEA_CNT6 pellets and (c) HEA_CNT3, HEA_CNT4, HEA_CNT5, HEA_CNT6 pellets.

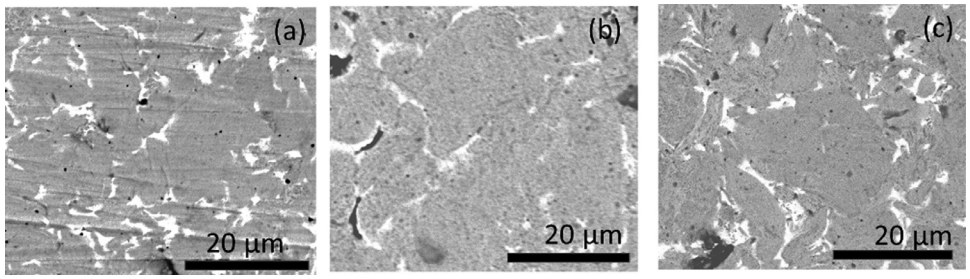

Fig. 9. Higher magnification SEM images showing phase contrast in (a) HEA, (b) HEA_CNT6 and (c) HEA_CNT9 samples.

re-appears. This aspect is more clearly visible in Fig. 9 which provides the BSE images of HEA, HEA_CNT6 and HEA_CNT9 pellets. The increase in the carbide phase is also noted in the BSE micrographs (by arrow). With the addition of CNTs, the F2 Cu-rich phase reduced and reached a minimum till HEA_CNT6 indicating homogenization. After this optimum concentration, large amounts of chromium carbide formed and Cu-rich phase re-appeared and increased with CNT content. The deconvoluted XRD peaks of HEA, HEA_CNT6, HEA_CNT9 samples together with average spot EDS analysis results of different regions are summarised in Fig. 10(a) and (b) respectively. Fig. 10(a) clearly shows the homogenization has led to the dissolution of two different fcc phases (in case of HEA sample) into a nearly single fcc phase microstructure (for HEA_CNT6 sample) while a comparison of the XRD curve for the HEA_CNT6 and HEA_CNT9 sample shows that increase in the CNT content has led to re-appearance of the two different fcc phases along with the chromium carbide phase. The average composition histogram clearly shows that a

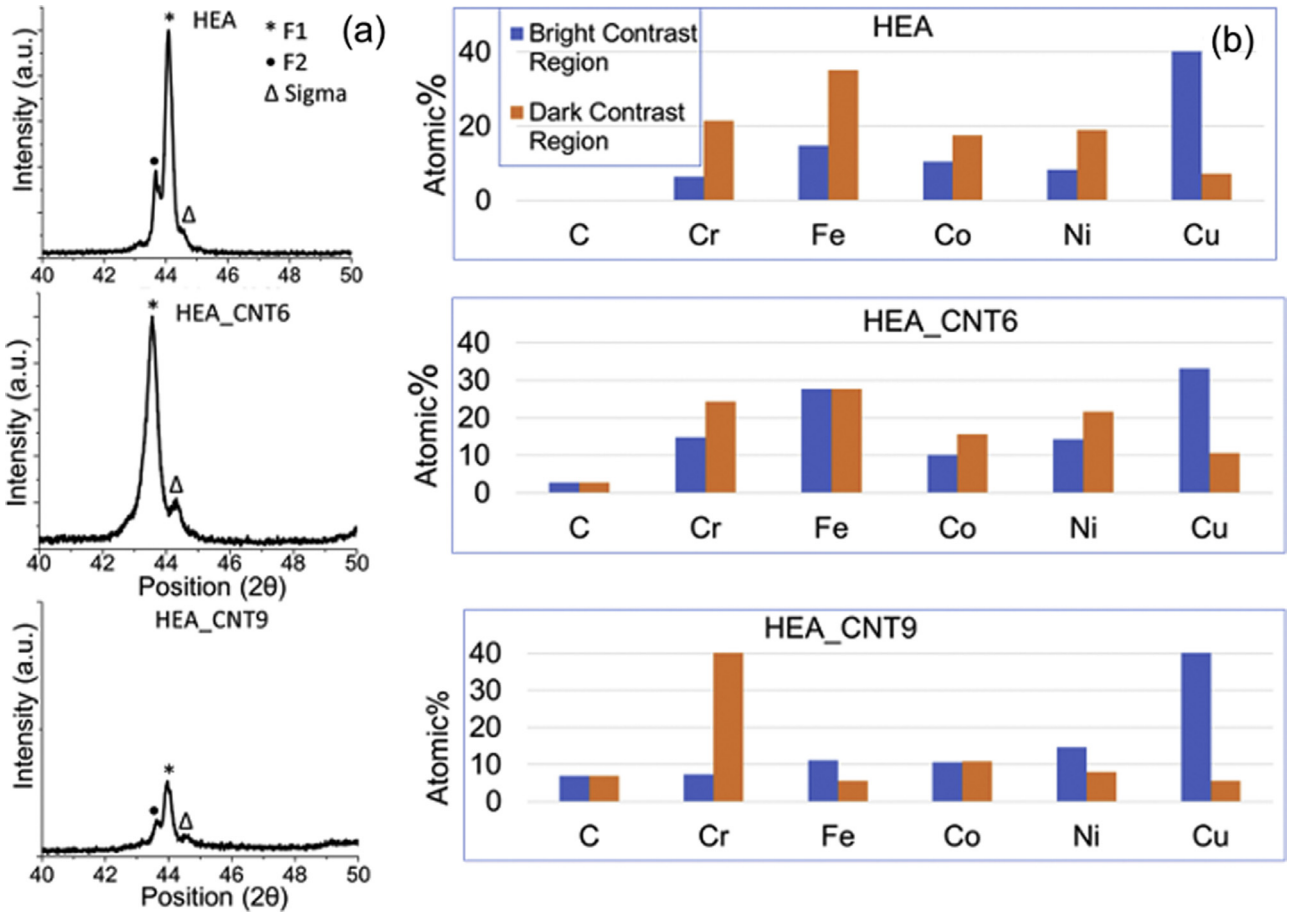

Fig. 10. (a) Deconvoluted XRD profiles of HEA, HEA_CNT6 and HEA_CNT9 pellets and (b) histogram plot obtained from several spot EDS analysis results from different regions in HEA, HEA_CNT6, HEA_CNT9 samples.

Table 4
Electrochemical parameters obtained from corrosion test.

Sample/ Parameters	E_{corr} (V)	i_{corr}(μA/cm^2)	Corrosion Rate(mil/year/cm^2)	ßc (mV/dec)	ßa (mV/dec)
HEA	-0.984	49.43	4.58	22.54	25.49
HEA_CNT1	-0.907	31.14	2.88	15.96	19.92
HEA_CNT2	-0.932	19.24	1.78	17.79	13.66
HEA_CNT3	-0.833	11.64	1.16	17.95	15.52
HEA_CNT4	-0.752	10.48	0.97	21.64	19.13
HEA_CNT5	-0.625	0.813	0.75	19.13	14.18
HEA_CNT6	-0.651	0.562	0.52	17.54	12.91
HEA_CNT7	-0.968	51.08	4.73	18.81	29.46
HEA_CNT8	-1.041	62.7	5.81	19.26	19.57
HEA_CNT9	-1.031	124.0	11.50	18.83	20.69

relatively higher compositional uniformity is achieved for the HEA_CNT6 sample when compared to the other two samples.

4. Corrosion analysis

Corrosion behaviour of pristine HEA and HEA-CNT composite pellets was determined using Tafel polarization studies in 3.5% NaCl medium. Tafel tests were performed by polarizing the working electrode ± 400 mV from the respective open circuit potential values. Tafel polarization curves obtained are shown in Fig. 11. Electrochemical parameters derived from the corrosion tests are tabulated in Table 4.

The corrosion current density (i_{corr}) (Eq. (1)) and corrosion rate (CR) (Eq. (2)) were calculated from the obtained parameter values using the following equations [31].

$$R_p = \frac{\beta_a \beta_c}{2.303\, i_{corr}\left(\beta_a + \beta_c\right)} \quad (1)$$

$$CR(mpy) = \frac{0.129 \times i_{corr} \times (E.W)}{d} \quad (2)$$

Where, i_{corr} is the corrosion current density, $\mu A/cm^2$; *EW* is the equivalent weight of system in grams and *d* is the density. Non-symmetrical tafel curves ($|\beta_a| \neq |\beta_c|$) suggest corrosion of the system. With CNT addition, $|\beta_a|$ exhibits higher values compared to $|\beta_c|$, which indicates that corrosion occurred due to anodic polarization.

Corrosion potential (E_{corr} in Table 4) for HEA sample was observed to be -0.984 V. Addition of CNTs in HEA resulted in positive shift/increase in the corrosion potential to -0.651 V (for HEA_CNT6) and with continued CNT addition it decreased to -1.030 V (for HEA_CNT9) indicating an improvement in the corrosion resistance followed by a deteriora-

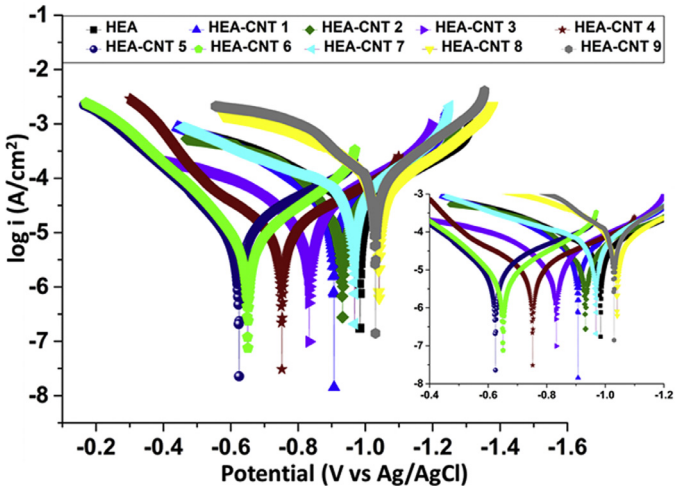

Fig. 11. Tafel polarisation curves of HEA and HEA-CNT composite pellets.

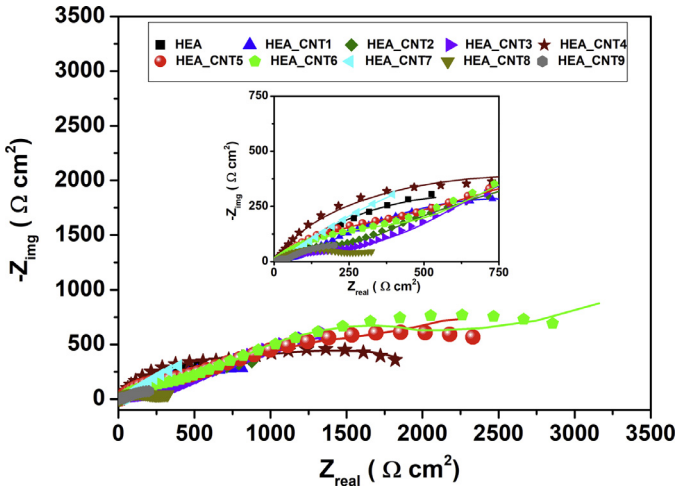

Fig. 12. Nyquist plots of HEA and HEA-CNT composite pellets (line: measured data, symbol: simulated data).

tion thereafter. Additionally, a decrease in i_{corr} value from HEA (49.43 μA/cm^2) to HEA-CNT6 (0.56 μA/cm^2) was observed. After HEA_CNT6, there was an increase in i_{corr} value from HEA_CNT7 (51.08 μA/cm^2) to HEA_CNT9 (124 μA/cm^2). This observation is also substantiated by decrease in corrosion rate from 4.58 mil/yr/cm^2 for HEA to 0.52 mil/yr/cm^2 for HEA_CNT6 (88.6% decrease) and a further rise from 4.73 mil/yr/cm^2 for HEA_CNT7 till 11.50 mil/yr/cm^2 for HEA_CNT9 (58% increase). An increase in corrosion potential with simultaneous decrease in corrosion current is an indicative of significantly improved corrosion resistance of the CNT incorporated HEA system. The increase in corrosion resistance property up to HEA_CNT6 and thereafter decrease in the resistance suggests that an optimum concentration of CNTs in HEA is required to achieve high corrosion resistance performance.

The EIS technique was used to understand the interfacial interaction of the pellets with the corrosive medium. All the measurements were conducted with the sinusoidal amplitude of 5 mV between the frequency range of 10 mHz - 100 kHz. The Nyquist plots and the Bode plots obtained are shown in the Figs. 12 and 13, respectively. Nyquist impedance plots show two capacitive loop for the samples except HEA-CNT4, HEA-CNT5 and HEA-CNT6, but HEA-CNT4, HEA-CNT5 and HEA-CNT6 show three capacitive loops and it can be clearly observed in phase angle versus log frequency Bode plot (Fig. 13(b)). The Nyquist plot (Fig. 12) shows that the diameter of the semicircle increases up to HEA-CNT6 sample after which it again starts to decrease indicating increase in corrosion resistance up to HEA-CNT6 followed by a decrease in the anti-corrosive property for the HEA with higher CNT incorporation. Fig. 13(a) reveals that increase in the amount of CNT in HEA causes increase in the impedance |Z| value. Also, with increase in the CNT content, the second time constant peak in phase angle versus log frequency plot shifts towards higher frequency (except HEA_CNT4) compared to HEA. All these observations indicate that with the increase in the amount of CNT, there is formation of protective barrier between pellet surface and the electroactive media which further reduces the corrosion process by reducing the active surface area.

The impedance parameters were obtained by fitting the experimentally determined EIS plots with electrical equivalent circuit (EEC) model using the Zsimpwin3.21 software. The circuit in Fig. 14(a) was used to fit the measured EIS data of all the samples except HEA-CNT4, HEA-CNT5 and HEA-CNT6 samples. The EIS data of HEA-CNT4, HEA-CNT5 and HEA-CNT6 samples was fitted with Fig. 14(b). In the used EECs, constant phase element (CPE) defined as 'Q' was used to replace the capacitance elements to take account of the porous corrosion products or inhomogeneities on the pellet surface. The CPE impedance is defined as (Eq. (3))

$$Z_{CPE} = 1/Q(jw)^n \quad (3)$$

Where Q is CPE constant, j is imaginary unit, $\omega = 2\pi f$ (f is the frequency), n is CPE exponent ($0 \le n \le 1$). In the EEC, R_s represents the solution resistance between the surface of the working electrode and the reference electrode. In Fig. 14(a) the high frequency contribution (R_1) and low frequency resistance (R_2) are attributed to the resistance due to the ionic leakage through the pores and charge transfer resistance respectively. Q_1 refers to the capacitance which represents the dielectric character of thin surface layer formed from the corrosion products at the electrolyte and working electrode interface and the low frequency contribution Q_2 is attributed to the double layer capacitance at the electrode surface. In Fig. 14(b) the high frequency contribution (R_1 and Q_1) are attributed to the resistance to ionic leakage and dielectric character of thin corrosion products layer at the working electrode, middle frequency elements (R_2 and Q_2) represents the charge transfer resistance and the double layer capacitance at the electrolyte and working electrode interface. The low frequency contribution (R_3 and Q_3) are attributed to the redox process taking place in the accumulated thin layer of the corrosion products on the electrode surface and electrolyte interface. For corrosion resistance evaluation, R_p can be expressed as $R_p = R_1 + R_2 + R_3$ from the EEC model shown in Fig. 14(a) and (b).

The obtained corrosion parameters from the EEC simulation of EIS data are given in Table 5. The charge transfer resistance R_2 is closely related to the corrosion rate of the material, the increase in charge transfer resistance means the higher corrosion resistance of the material. An increase in R_2 value and a corresponding decrease in Q_2 value (till HEA_CNT6) can be noted. The R_1 value increases and corresponding Q_1 value decreases because of increased difficulty in penetration of the corrosive media through the thin layer of corrosion products. The increase in R_2 and decrease in double layer capacitance Q_2 value with increase in the CNT content of the sample represents the decreased in surface activity. As the corrosion progresses, there is formation of thicker corrosion products layer on HEA-CNT4, HEA-CNT5 and HEA-CNT6, which further reduces the contact between corrosive media and the pellet surface. This stable corrosion products layer with CNT provided more resistance to the corrosion process at the surface of HEA-CNT5, HEA-CNT6 and HEA-CNT6. The polarization resistance, R_p which is directly proportional to the corrosion resistance of the material increases from HEA to HEA-CNT6 samples and decreases for the samples HEA-CNT7, HEA-CNT8 and HEA-CNT9 and it resembles with the corrosion behavior of the samples observed in the potentiodynamic polarization study. The R_p value follows the same trend emphasising that there exists an optimum with respect to amount of CNT to achieve high corrosion resistance property.

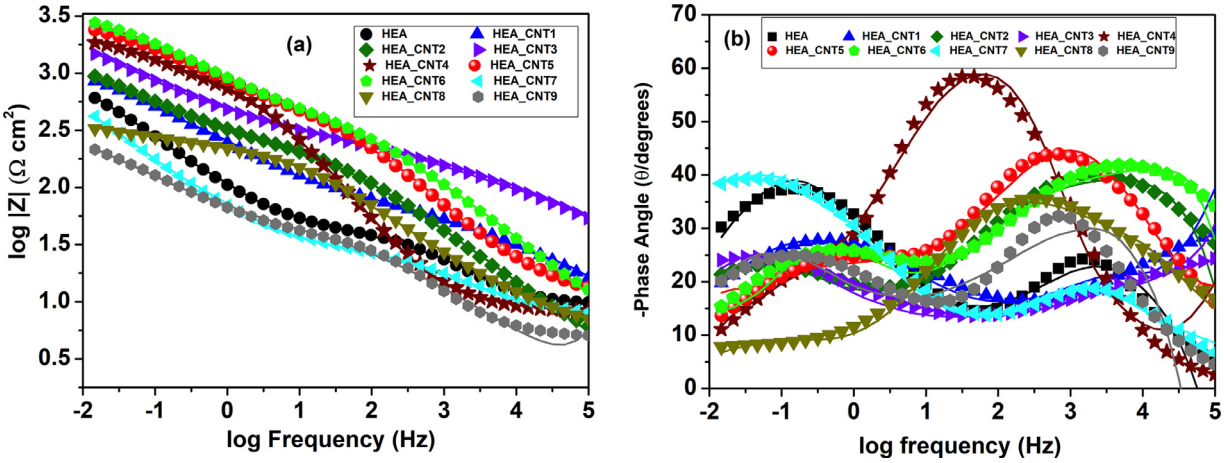

Fig. 13. **(a)** log frequency Vs log |Z| and **(b)** log frequency Vs phase angle Bode plots of HEA and HEA-CNT composite pellets (line: measured data, symbol: simulated data).

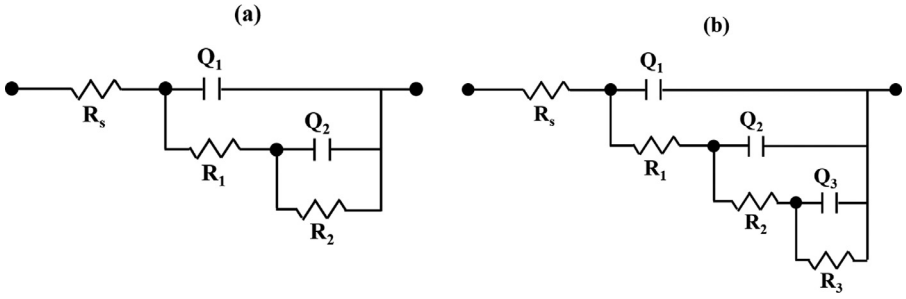

Fig. 14. Electrochemical equivalent circuits (EECs) used for simulation of **(a)** HEA, HEA_CNT1, HEA_CNT2, HEA_CNT3, HEA_CNT7, HEA_CNT8 and HEA_CNT9 and **(b)** HEA_CNT4, HEA_CNT5 and HEA_CNT6 EIS data.

Table 5
Sample parameters values obtained from EEC simulation of EIS data.

Samples/ Parameters	R_s Ω cm^2	Q_1 10^{-3} ($\Omega^{-1}cm^{-2}S^{-n}$)	n_1	R_1 Ω cm^2	Q_2 10^{-3} ($\Omega^{-1}cm^{-2}S^{-n}$)	n_2	R_2 Ω cm^2	Q_3 10^{-6} ($\Omega^{-1}cm^{-2}S^{-n}$)	n_3	R_3 Ω cm^2	R_p Ω cm^2	Chi square E^{-3}
HEA	9.3	0.98	0.69	30	4.42	0.56	595				625	3.76
HEA_CNT1	4.3	0.28	0.4	82	1.7	0.46	791				873	1.87
HEA_CNT2	3.3	0.13	0.57	192	2.5	0.31	819				1011	1.50
HEA_CNT3	9.7	0.22	0.8	295	1.4	0.8	1216				1511	0.93
HEA_CNT4	10	0.44	0.37	90.6	0.51	0.8	1011	3.2	076	1048	2068	1.63
HEA_CNT5	9.1	0.015	0.84	434	0.58	0.76	1376	6.63	0.81	637	2447	0.35
HEA_CNT6	4.5	0.07	0.68	542	0.4	0.8	1472	0.41	0.86	1140	3154	2.29
HEA_CNT7	7.2	0.39	0.56	31	7.4	0.82	360				391	0.41
HEA_CNT8	5.1	0.48	0.5	209	37.6	0.83	132				341	0.56
HEA_CNT9	5.2	0.086	0.78	42	9.5	0.31	186				228	2.46

5. Conclusions

Nanostructured FeNiCoCrCu-CNT composites were produced by MA-SPS route. A major FCC with a minor BCC phase formed in the multicomponent metal powder blend after 30 hours of milling. After sintering, BCC phase transformed to σ phase and two other FCC phases evolved. Beyond the optimum CNT concentration (2 wt.% CNT), large amount of chromium carbide phase also formed in the composite pellets. Sintering of HEA and HEA_CNT powders led to an increase in the crystallite size and reduction in the lattice strain due to recovery and recrystallization of the severely deformed milled microstructures. The addition of CNTs impeded these processes, and therefore grain size in HEA-CNT composites were smaller and lattice strain values were higher when compared to the HEA pellets. Microstructural characterization revealed that with the initial addition of CNTs, microstructural homogeneity was achieved. While for higher CNT additions, high volume fraction of chromium carbide phase formed which also led to re-evolution of phase inhomogeneity.

Corrosion resistance behavior of the pellets was highly sensitive to the amount of CNTs contained in them. The corrosion rate substantially decreased with initial addition of CNT to reach a minimum. Beyond this, the corrosion rate increased with continued addition of CNTs. This showed that there exists an optimum amount of CNT that can be incorporated in the HEA matrix to achieve substantially high corrosion resistance performance. Between the pristine HEA pellet and the pellet with optimum CNT amount (2 wt.%), 88.6 % reduction in the corrosion rate was measured. Improvement in the corrosion resistance was attributed to the enhancement in the chemical homogeneity which reduced the possibility of galvanic coupling. Increase in the corrosion rate beyond the optimum CNT was attributed to the re-appearance of chemical heterogeneity and evolution of $Cr_{23}C_6$ phase.

Declaration of Competing Interest

None

Acknowledgement

The authors acknowledge the research funding received from the SERB Government of India.

References

[1] J.W. Yeh, Recent progress in high entropy alloys, Ann. Chim. Sci. Mater. 31 (2006) 633–648.
[2] Y. Zhang, T.T. Zuo, Z. Tang, M.C. Gao, K.A. Dahmen, P.K. Liaw, Z.P. Lu, Microstructures and properties of high-entropy alloys, Prog. Mater. Sci. 61 (2014) 1–93.
[3] B.S. Murty, J.W. Yeh, S. Ranganathan, High-Entropy Alloys Butterworth-Heinemann, Elsevier, London, England, 2014.
[4] J.H. Zhao, X.L. Ji, Y.P. Shan, Y. Fu, Z. Yao, On the microstructure and erosion–corrosion resistance of AlCrFeCoNiCu high-entropy alloy via annealing treatment, Mater. Sci. Technol. 32 (2016) 1271–1276.
[5] T.M. Butler, J.P. Alfano, R.L. Martens, M.L. Weaver, High temperature oxidation behavior of Al–Co–Cr–Ni–(Fe or Si) multicomponent high-entropy alloys, JOM 67 (2015) 246–259.
[6] G. Laplanche, U.F. Volkert, G. Eggeler, E.P. George, Oxidation behavior of the CrMnFeCoNi high-entropy alloy, Oxid. Metals. 85 (2016) 629–645.
[7] M. Yang, X.J. Liu, H.H. Ruan, Y. Wu, H. Wang, Z.P. Lu, High thermal stability and sluggish crystallization kinetics of high-entropy bulk metallic glasses, J. Appl. Phys. 119 (2016) 245112–245119.
[8] W.Y. Tang, J.W. Yeh, Effect of aluminium content on plasma-nitrided Al_xCoCrCuFeNi high-entropy alloys, Metall. Mater. Trans. A 40 (2009) 1479–1486.
[9] Z. Li, K.G. Pradeep, Y. Deng, D. Raabe, C.C. Tasan, Metastable high-entropy dual-phase alloys overcome the strength–ductility trade-off, Nature 534 (2016) 227–230.
[10] B. Gludovatz, A. Hohenwarter, D. Catoor, E.H. Chang, E.P. George, R.O. Ritchie, A fracture-resistant high-entropy alloy for cryogenic applications, Science 345 (2014) 1153–1158.
[11] Varalakshmi, M. Kamaraj, B.S. Murty, Synthesis and characterization of nanocrystalline AlFeTiCrZnCu high entropy solid solution by mechanical alloying, J. Alloys Compd. 460 (2008) 253–257.
[12] B. Kang, J. Lee, H.J. Ryu, S.H. Hong, Microstructure, mechanical property and Hall–Petch relationship of a lightweight refractory $Al_{0.1}$CrNbVMo high entropy alloy fabricated by powder metallurgical process, J. Alloys Compd. 767 (2018) 1012–1021.
[13] M. Murali, S.P. Kumaresh Babu, J. Majhi, A. Vallimanalan, R. Mahendran, Processing and characterization of nanocrystalline AlCoCrCuFeTi$_x$ high-entropy alloy, Powder Metall 61 (2018) 139–148.
[14] S. Praveen, B.S. Murty, R.S. Kottada, Alloying behavior in multi-component AlCoCrCuFe and NiCoCrCuFe high entropy alloys, Mater. Sci. Eng. A 534 (2012) 83–89.
[15] R.M. Pohan, B. Gwalani, J. Lee, T. Alam, J.Y. Hwang, H.J. Ryu, R. Banerjee, S.H. Hong, Microstructures and mechanical properties of mechanically alloyed and spark plasma sintered $Al_{0.3}$CoCrFeMnNi high entropy alloy, Mater. Chem. Phys. 210 (2018) 62–70.
[16] A. Kumar, A.K. Swarnakar, M. Chopkar, Phase evolution and mechanical properties of AlCoCrFeNiSi$_x$ high entropy alloys synthesized by mechanical alloying and spark plasma sintering, J. Mater. Eng. Perform. 27 (2018) 3304–3314.
[17] S. Praveen, B.S. Murty, Ravi S. Kottada, Phase evolution and densification behavior of nanocrystalline multicomponent high entropy alloys during spark plasma sintering, JOM 65 (2013) 1797–1804.
[18] A. Shabani, M. Reza, T.A. Shafyei, R.E. Loge, Evaluation of mechanical properties of the heat treated FeCrCuMnNi high entropy alloys, Mater. Chem. Phys. 221 (2019) 68–77.
[19] A. Munitz, M.J. Kaufman, M. Nahmany, N. Derimow, R. Abbaschian, Microstructure and mechanical properties of heat treated $Al_{1.25}$CoCrCuFeNi high entropy alloys, Mater. Sci. Eng. A 714 (2018) 146–159.
[20] S-C. Her, C-Y. Lai, Synthesis and characterization of functionalized multi-walled carbon nanotubes, Appl. Mech. Mater. 307 (2013) 377–380.
[21] I. Firkowska, A. Boden, A.-M. Vogt, S. Reich, Effect of carbon nanotube surface modification on thermal properties of copper–CNT composites, J. Mater. Chem. 21 (2011) 17541–17546.
[22] S.M. Uddin, T. Mahmud, C. Wolf, C. Glanz, I. Kolaric, C. Volkmer, H. Höller, l. Wienecke, S. Roth, H.-J. Fecht, Effect of size and shape of metal particles to improve hardness and electrical properties of carbon nanotube reinforced copper and copper alloy composites, Comp. Sci. Technol. 70 (2010) 2253–2257.
[23] M.F. Yu, O. Lourie, M.J. Dyer, K. Moloni, T.F. Kelly, R.S. Ruoff, Strength and breaking mechanism of multiwalled carbon nanotubes under tensile load, Science 287 (2000) 637–640.
[24] A. Almajid, L. Bendler, K. Friedrich, B. Wetzel, Effects of graphene and CNT on mechanical, thermal, electrical, and corrosion properties of vinylester based nanocomposites, Plastics Rubber Comp. 44 (2015) 50–62.
[25] V. Singh, R. Diaz, K. Balani, A. Agarwal, S. Seal Chromium carbide–CNT nanocomposites with enhanced mechanical properties, Acta Mater 57 (2009) 335–344.
[26] S. Azadehranjbar, F. Karimzadeh, M.H. Enayati, Development of NiFe-CNT and Ni_3Fe-CNT nanocomposites by mechanical alloying, Adv. Powder Technol. 23 (2012) 338–342.
[27] X.H. Chen, C. Chen, H.N. Xiao, F.Q. Cheng, G.Z. Zhang, G.J. Yi, Corrosion behavior of carbon nanotubes–Ni composite coating, Surf. Coatings Technol. 191 (2005) 351–356.
[28] M. Alishahi, S. Hosseini, S.M. Monirvaghefi, A. Saatchi, The effect of carbon nanotubes on the corrosion and tribological behavior of electroless Ni–P–CNT composite coating, Appl. Surf. Sci. 258 (2012) 2439–2446.
[29] N.N. Aung, W. Zhou, C.S. Goh, S.M.L. Nai, J. Wei, Effect of carbon nanotubes on corrosion of Mg–CNT composites, Corros. Sci. 52 (2010) 1551–1553.
[30] P. Gill, N. Munroe, Study of carbon nanotubes in Cu-Cr metal matrix composites, J. Mater. Eng. Perform. 21 (2012) 2467–2471.
[31] B.M. Praveen, T.V. Venkatesha, Electrodeposition and properties of Zn–Ni–CNT composite coatings, J. Alloys and Compd. 482 (2009) 53–57.
[32] S. Arora, N. Kumari, C. Srivastava, Microstructure and Corrosion behavior of NiCo – Carbon Nanotube composite coatings, J. Alloys Compd. 801 (2019) 449–459.
[33] P.M. Kibasomba, S. Dhlamini, M. Maaza, C.-P. Liu, M.M. Rashad, D.A. Rayan, B.W. Mwakikunga, Strain and grain size of TiO_2 nanoparticles from TEM, Raman spectroscopy and XRD: The revisiting of the Williamson-Hall plot method, Results Phys. 9 (2018) 628–635.
[34] R. Das, S.B.A. Hamid, M.E. Ali, S. Ramkrishna, W. Yongzhi, Carbon nanotubes characterization by x-ray powder diffraction – a review, Current Nanosci. 11 (1) (2015).
[35] E. Titus, N. Ali, G. Cabral, J. Gracio, P. Ramesh Babu, M.J. Jackson, Chemically functionalized carbon nanotubes and their characterisation using thermogravimetric analysis, fourier transform infrared, and Raman spectroscopy, J. Mech. Eng. Perform. 15 (2006) 182–186.
[36] G.A. Rance, D.H. Marsh, R.J. Nicholas, A.N. Khlobystov, UV-vis absorption Spectroscopy of carbon nanotubes: Relationship between the π-electron plasmon and nanotube diameter, Chem. Phys. Lett. 493 (2010) 19–23.
[37] K.B. Zhang, Z.Y. Fu, J.Y. Zhang, J. Shi, W.M. Wang, H. Wang, Y.C. Wang, Q.J. Zhang, Nanocrystalline CoCrFeNiCuAl high-entropy solid solution synthesized by mechanical alloying, J. Alloys Compd. 485 (2009) L31–L34.
[38] K. Zhang, Z. Fu, J. Zhang, W. Wang, H. Wang, Y. Wang, Q. Zhang, Characterization of nanocrystalline CoCrFeNiCuAl high-entropy alloy powder processed by mechanical alloying, Mater. Sci. Forum 620-622 (2009) 383–386.
[39] V. Shivam, J. Basu, V.K. Pandey, Y. Shadangi, N.K. Mukhopadhyay, Alloying behaviour, thermal stability and phase evolution in quinary AlCoCrFeNi high entropy alloy, Adv. Power Technol. 29 (9) (2018) 2221–2230.
[40] Y.L. Chen, Y.H. Hu, C.A. Hsieh, J.W. Yeh, S.K. Chen, Competition between elements during mechanical alloying in an octonary multi-principal-element alloy system, J. Alloy Compd. 481 (2009) 768–775.
[41] S. Praveen, B.S. Murty, R.S. Kottada, Alloying behavior in multi-component AlCoCrCuFe and NiCoCrCuFe high entropy alloys, Mater. Sci. Eng. A 534 (2012) 83–89.
[42] A. Arab, Y. Guo, Q. Zhou, P. Chen, Fabrication of nanocrystalline AlCoCrFeNi high entropy alloy through shock consolidation and mechanical alloying, Entropy 21 (9) (2019) 880 (1-12).
[43] M. Vaidya, M.M. Garalpati, B.S. Murthy, High entropy alloys by mechanical alloying: a review, J. Mater. Res. 34 (5) (2019) 664–686.